



**HAL**  
open science

# Spatial resolution versus contrast trade-off enhancement in high-resolution surface plasmon resonance imaging (SPRI) by metal surface nanostructure design

F. Banville, Julien Moreau, Mitradeep Sarkar, Mondher Besbes, Michael Canva, Paul Charette

## ► To cite this version:

F. Banville, Julien Moreau, Mitradeep Sarkar, Mondher Besbes, Michael Canva, et al.. Spatial resolution versus contrast trade-off enhancement in high-resolution surface plasmon resonance imaging (SPRI) by metal surface nanostructure design. *Optics Express*, 2018, 26 (8), pp.10616. 10.1364/OE.26.010616 . hal-01757515

**HAL Id: hal-01757515**

**<https://hal-iogs.archives-ouvertes.fr/hal-01757515>**

Submitted on 16 Dec 2020

**HAL** is a multi-disciplinary open access archive for the deposit and dissemination of scientific research documents, whether they are published or not. The documents may come from teaching and research institutions in France or abroad, or from public or private research centers.

L'archive ouverte pluridisciplinaire **HAL**, est destinée au dépôt et à la diffusion de documents scientifiques de niveau recherche, publiés ou non, émanant des établissements d'enseignement et de recherche français ou étrangers, des laboratoires publics ou privés.



# Spatial resolution versus contrast trade-off enhancement in high-resolution surface plasmon resonance imaging (SPRI) by metal surface nanostructure design

FREDERIC A. BANVILLE,<sup>1,2,3</sup> JULIEN MOREAU,<sup>3</sup> MITRADEEP SARKAR,<sup>3</sup>  
MONDHER BESBES,<sup>3</sup> MICHAEL CANVA,<sup>1,2,3</sup> AND PAUL G. CHARETTE<sup>1,2,\*</sup>

<sup>1</sup>Laboratoire Nanotechnologies Nanosystèmes (LN2)- CNRS UMI-3463, Université de Sherbrooke, Sherbrooke J1K 0A5, Canada

<sup>2</sup>Institut Interdisciplinaire d'Innovation Technologique (3IT), Université de Sherbrooke, Sherbrooke J1K 0A5, Canada

<sup>3</sup>Laboratoire Charles Fabry, Institut d'Optique Graduate School, Université Paris-Saclay, CNRS, Palaiseau 91127, France

\*Paul.G.Charette@USherbrooke.ca

**Abstract:** Surface plasmon resonance imaging (SPRI) is an optical near-field method used for mapping the spatial distribution of chemical/physical perturbations above a metal surface without exogenous labeling. Currently, the majority of SPRI systems are used in microarray biosensing, requiring only modest spatial resolution. There is increasing interest in applying SPRI for label-free near-field imaging of biological cells to study cell/surface interactions. However, the required resolution (sub- $\mu\text{m}$ ) greatly exceeds what current systems can deliver. Indeed, the attenuation length of surface plasmon polaritons (SPP) severely limits resolution along one axis, typically to tens of  $\mu\text{m}$ . Strategies to date for improving spatial resolution result in a commensurate deterioration in other imaging parameters. Unlike the smooth metal surfaces used in SPRI that support purely propagating surface modes, nanostructured metal surfaces support “hybrid” SPP modes that share attributes from both propagating and localized modes. We show that these hybrid modes are especially well-suited to high-resolution imaging and demonstrate how the nanostructure geometry can be designed to achieve sub- $\mu\text{m}$  resolution while mitigating the imaging parameter trade-off according to an application-specific optimum.

© 2018 Optical Society of America under the terms of the [OSA Open Access Publishing Agreement](#)

**OCIS codes:** (240.6680) Surface plasmons; (310.6628) Subwavelength structures, nanostructures; (110.0110) Imaging systems; (000.4430) Numerical approximation and analysis; (180.4243) Near-field microscopy.

## References and links

1. E. Kretschmann and H. Raether, “Notizen: Radiative Decay of Non Radiative Surface Plasmons Excited by Light,” *Z. Für Naturforschung A*, **23**, 2135–2136 (1968).
2. A. Otto, “Excitation of nonradiative surface plasma waves in silver by the method of frustrated total reflection,” *Z. Fr Phys. Hadrons Nucl.* **216**, 398–410 (1968).
3. S. Lal, S. Link, and N. J. Halas, “Nano-optics from sensing to waveguiding,” *Nat. Photonics* **1**, 641–648 (2007).
4. J. Homola, S. S. Yee, and G. Gauglitz, “Surface Plasmon Resonance Based Sensors,” *Sens. Actuat. B Chem.* **54**, 3–15 (1999).
5. H. E. de Bruijn, R. P. H. Kooyman, and J. Greve, “Surface plasmon resonance microscopy: improvement of the resolution by rotation of the object,” *Appl. Opt.* **32**(13), 2426–2430 (1993).
6. C. E. H. Berger, R. P. H. Kooyman, and J. Greve, “Resolution in surface plasmon microscopy,” *Rev. Sci. Instrum.* **65**, 2829–2836 (1994).
7. K. Giebel, C. Bechinger, S. Herminghaus, M. Riedel, P. Leiderer, U. Weiland, and M. Bastmeyer, “Imaging of Cell/Substrate Contacts of Living Cells with Surface Plasmon Resonance Microscopy,” *Biophys. J.* **76**(1 Pt 1), 509–516 (1999).
8. L. Laplatine, L. Leroy, R. Calemczuk, D. Baganizi, P. N. Marche, Y. Roupioz, and T. Livache, “Spatial resolution in prism-based surface plasmon resonance microscopy,” *Opt. Express* **22**(19), 22771–22785 (2014).
9. B. Huang, F. Yu, and R. N. Zare, “Surface Plasmon Resonance Imaging Using a High Numerical Aperture Microscope Objective,” *Anal. Chem.* **79**(7), 2979–2983 (2007).

10. T. Söllradl, F. A. Banville, V. Chabot, M. Canva, M. Grandbois, and P. G. Charette, "Metal clad waveguide (MCWG) based imaging using a high numerical aperture microscope objective," *Opt. Express* **25**(3), 1666–1679 (2017).
11. E. M. Yeatman, "Resolution and sensitivity in surface plasmon microscopy and sensing," *Biosens. Bioelectron.* **11**, 635–649 (1996).
12. H. Raether, *Surface Plasmons on Smooth and Rough Surfaces and on Gratings* (Springer, 2006), Vol. 111.
13. F. A. Banville, T. Söllradl, P.-J. Zermatten, M. Grandbois, and P. G. Charette, "Improved resolution in SPR and MCWG microscopy by combining images acquired with distinct mode propagation directions," *Opt. Lett.* **40**(7), 1165–1168 (2015).
14. S.-H. Kim, W. Chegal, J. Doh, H. M. Cho, and D. W. Moon, "Study of cell-matrix adhesion dynamics using surface plasmon resonance imaging ellipsometry," *Biophys. J.* **100**(7), 1819–1828 (2011).
15. K. Watanabe, K. Matsuura, F. Kawata, K. Nagata, J. Ning, and H. Kano, "Scanning and non-scanning surface plasmon microscopy to observe cell adhesion sites," *Biomed. Opt. Express* **3**(2), 354–359 (2012).
16. A. W. Peterson, M. Halter, A. Tona, and A. L. Plant, "High resolution surface plasmon resonance imaging for single cells," *BMC Cell Biol.* **15**, 35 (2014).
17. K. Toma, H. Kano, and A. Offenhäuser, "Label-Free Measurement of Cell-Electrode Cleft Gap Distance with High Spatial Resolution Surface Plasmon Microscopy," *ACS Nano* **8**(12), 12612–12619 (2014).
18. T. Söllradl, F. A. Banville, U. Fröhlich, M. Canva, P. G. Charette, and M. Grandbois, "Label-free visualization and quantification of single cell signaling activity using metal-clad waveguide (MCWG)-based microscopy," *Biosens. Bioelectron.* **100**, 429–436 (2018).
19. P. Y. Liu, L. K. Chin, W. Ser, H. F. Chen, C.-M. Hsieh, C.-H. Lee, K.-B. Sung, T. C. Ayi, P. H. Yap, B. Liedberg, K. Wang, T. Bourouina, and Y. Leprince-Wang, "Cell refractive index for cell biology and disease diagnosis: past, present and future," *Lab Chip* **16**(4), 634–644 (2016).
20. M. G. Somekh, S. Liu, T. S. Velinov, and C. W. See, "High-resolution scanning surface-plasmon microscopy," *Appl. Opt.* **39**(34), 6279–6287 (2000).
21. L. Berguiga, L. Streppa, E. Boyer-Provera, C. Martinez-Torres, L. Schaeffer, J. Elezgaray, A. Arneodo, and F. Argoul, "Time-lapse scanning surface plasmon microscopy of living adherent cells with a radially polarized beam," *Appl. Opt.* **55**(6), 1216–1227 (2016).
22. K. Watanabe, R. Miyazaki, G. Terakado, T. Okazaki, K. Morigaki, and H. Kano, "High resolution imaging of patterned model biological membranes by localized surface plasmon microscopy," *Appl. Opt.* **49**(5), 887–891 (2010).
23. S. Collin, "Nanostructure arrays in free-space: optical properties and applications," *Rep. Prog. Phys.* **77**(12), 126402 (2014).
24. Y. Zeng, R. Hu, L. Wang, D. Gu, J. He, S.-Y. Wu, H.-P. Ho, X. Li, J. Qu, B. Z. Gao, and Y. Shao, "Recent advances in surface plasmon resonance imaging: detection speed, sensitivity, and portability," *Nanophotonics* **6**, 1017–1030 (2017).
25. R. Gillibert, M. Sarkar, J.-F. Bryche, R. Yasukuni, J. Moreau, M. Besbes, G. Barbillon, B. Bartenlian, M. Canva, and M. L. de la Chapelle, "Directional surface enhanced Raman scattering on gold nano-gratings," *Nanotechnology* **27**(11), 115202 (2016).
26. Y. Oh, T. Son, S. Y. Kim, W. Lee, H. Yang, J. R. Choi, J.-S. Shin, and D. Kim, "Surface plasmon-enhanced nanoscopy of intracellular cytoskeletal actin filaments using random nanodot arrays," *Opt. Express* **22**(22), 27695–27706 (2014).
27. D. J. Kim and D. Kim, "Subwavelength grating-based nanoplasmonic modulation for surface plasmon resonance imaging with enhanced resolution," *J. Opt. Soc. Am. B* **27**, 1252–1259 (2010).
28. M. Chamtour, A. Dhawan, M. Besbes, J. Moreau, H. Ghalila, T. Vo-Dinh, and M. Canva, "Enhanced SPR Sensitivity with Nano-Micro-Ribbon Grating—an Exhaustive Simulation Mapping," *Plasmonics* **9**, 79–92 (2014).
29. M. Chamtour, M. Sarkar, J. Moreau, M. Besbes, H. Ghalila, and M. Canva, "Field enhancement and target localization impact on the biosensitivity of nanostructured plasmonic sensors," *J. Opt. Soc. Am. B* **31**, 1223–1231 (2014).
30. M. Sarkar, M. Besbes, J. Moreau, J.-F. Bryche, A. Olivéro, G. Barbillon, A.-L. Coutrot, B. Bartenlian, and M. Canva, "Hybrid Plasmonic Mode by Resonant Coupling of Localized Plasmons to Propagating Plasmons in a Kretschmann Configuration," *ACS Photonics* **2**, 237–245 (2015).
31. M. Sarkar, J.-F. Bryche, J. Moreau, M. Besbes, G. Barbillon, B. Bartenlian, and M. Canva, "Generalized analytical model based on harmonic coupling for hybrid plasmonic modes: comparison with numerical and experimental results," *Opt. Express* **23**(21), 27376–27390 (2015).
32. M. Besbes, J. P. Hugonin, P. Lalanne, S. van Haver, O. T. A. Janssen, A. M. Nugrowati, M. Xu, S. F. Pereira, H. P. Urbach, A. S. van de Nes, P. Bienstman, G. Granet, A. Moreau, S. Helfert, M. Sukharev, T. Seideman, F. I. Baida, B. Guizal, and D. Van Labeke, "Numerical analysis of a slit-groove diffraction problem," *J. Eur. Opt. Soc.* **2**, 07022 (2007).
33. P. B. Johnson and R. W. Christy, "Optical Constants of the Noble Metals," *Phys. Rev. B* **6**, 4370–4379 (1972).
34. M. Daimon and A. Masumura, "Measurement of the refractive index of distilled water from the near-infrared region to the ultraviolet region," *Appl. Opt.* **46**(18), 3811–3820 (2007).

## 1. Introduction

Surface plasmon resonance (SPR) sensing is an optical near-field based method for detecting minute material or physical changes that occur within a thin volume on the dielectric side of a metal/dielectric interface [1, 2]. The literature often describes SPR sensing with a mixture of quantum mechanical (photons, plasmons, polaritons) and classical (electromagnetic waves, phase matching, evanescent fields) terminology. Except for single photons or entangled states, SPR can be entirely described by classical electromagnetism [3], which facilitates quantitative comparisons with other guided wave near-field optical sensing methods. SPR systems generally fall into two classes depending on the nature of the electromagnetic modes in play: “propagating” modes at smooth dielectric/metal planar interfaces versus “localized” modes at the surface of colloidal metal nanoparticles or nanostructured metal surfaces.

A typical propagating-type SPR sensor is in fact a planar waveguide that supports a single TM-polarized guided mode propagating at a metal/dielectric interface with a field profile that decays exponentially on either side, i.e. a surface wave. This mode, commonly referred to as “surface plasmon polaritons (SPP)” or simply as “surface plasmons”, can be excited by input light with a matching wavevector in a number of ways, similarly to guided modes in photonic waveguides. The “SPP mode” is attenuated over a short distance because, in standard photonics terminology, it is both “lossy” due to propagation losses by absorption in the metal and “leaky” due to out-coupling of guided light back into the high index medium of the input/output optical coupling system. Since mode characteristics and input/output coupling efficiency are highly dependent on local material properties and geometry, perturbations near the interface that change the dielectric refractive index distribution within the effective range of the evanescent field will induce variations in the output light intensity [4]. Resonance occurs when the uncoupled fraction of input light interferes destructively with light out-coupled from the SPP mode, causing the output intensity to drop to a minimum.

With appropriate optics and a 2D sensor (camera), propagating-type SPR can be used for imaging (SPRI), where refractive index variations in the dielectric close to the metal/dielectric interface are spatially resolved in the plane of the interface. Most SPRI systems use off-the-shelf equilateral prisms for input/output light coupling [5–7] where imaging resolution in the plane is typically several  $\mu\text{m}$  or more. Resolution can be improved by using custom-designed prisms to reduce geometric aberrations [8] or a high numerical aperture microscope objective for input/output optical coupling [9, 10]. Ultimately, spatial resolution in widefield (un-scanned) SPRI is limited by the “attenuation length” (defined below) in the mode propagation direction and by diffraction in the orthogonal direction [6, 10, 11]. As the attenuation length is typically greater than the diffraction limit, spatial resolution is anisotropic. This phenomenon is most apparent in high-resolution SPRI, where images appear to suffer from a “blurring effect” along the direction of mode propagation [12, 13].

Currently, the vast majority of SPRI systems are used with spotted microarrays for parallel measurements of affinity assays. In such cases, spatial resolution is not critical since a single averaged measurement is sought for each spot (typically  $100\ \mu\text{m}$  in diameter or more). Recently, there has been growing interest in real-time label-free surface-based (near-field) imaging of relatively large biological objects such as cells to better understand how interactions with the substrate may trigger specific biochemical signalling events that lead to pathological behavior, such as with many types of cancer. SPRI is particularly well suited to this challenging task and a number of groups have published pioneering work in this area [7, 14–17]. In this relatively new application of SPRI, spatial resolution *is* of critical importance. While most of the cell body is generally outside the evanescent field and thus out of SPR sensing range, the first hundred nanometers above the sensor surface are nevertheless “information rich” for key aspects of cell behavior such as focal adhesion remodelling during cell motility and morphological changes induced by molecular signalling events [18]. The relatively large refractive index differences ( $1.355 < n < 1.60$ ) between the cellular organelles and the cytosol (intra-cellular fluid), as well as between the organelles themselves [19], are

easily observable with SPR. However, focal adhesion and cytoskeleton remodelling involve fine (sub- $\mu\text{m}$ ) features both within the cells (organelles) and at the cell boundary (ex: pseudopods) that can only be resolved with high spatial resolution, where resolution anisotropy in SPRI is a significant problem.

Several approaches have been proposed to address the resolution problem along the mode propagation direction in SPRI. Scanning-based methods exploit SPP mode self-interference to achieve isotropic diffraction-limited imaging but at the cost of much longer image acquisition times [15, 17, 20–22]. Other approaches involve using higher loss metals [9] or numerically combining images with distinct mode propagation directions [13]. These techniques are, however, limited in either temporal resolution or image contrast.

Over the past decade, there have been many exciting developments in nanoplasmonics [23]. Most of the work to date applied to biosensing on planar substrates has focused on local enhancement of the electric field (“hot spots”) either to increase sensitivity at very low target concentrations [24] or for surface-enhanced Raman spectroscopy (SERS) [25], and more recently in super-resolution fluorescence microscopy [26]. Since label-free high-resolution imaging of distributed objects such as biological cells with SPRI is a fairly new field, relatively little work has been done so far to explore nanoplasmonics solutions to the spatial resolution anisotropy problem, with only a few notable exceptions [27]. In a series of papers published by our group on SPP modes supported by nanostructured metal films, we showed that strong coupling between propagating and localized modes gives rise to a “hybrid” SPP mode [28–31]. In continuation of this work, we demonstrate in the present paper that these hybrid modes are especially well suited for high resolution SPRI as they benefit from a reduction in attenuation length due to the localized component influence, thereby improving resolution along the direction of mode propagation, without undue deterioration in other performance metrics relative to a purely propagating mode. The particular balance between the propagating and localized mode properties is entirely determined by the metal surface nanostructure geometry and can be tailored according to application-specific design criteria.

The nanostructure design process, involving numerical modeling and parameter estimation from the experimental data, is described below in a case study based on one of the most common SPRI biosensing system configurations: a dielectric fluid medium atop a 50 nm uniform gold film at an operating wavelength of  $\lambda = 830$  nm. This particular choice of wavelength is motivated by the fact that longer operating wavelengths yield higher SPR sensitivity and that 830 nm is considered the practical upper limit for systems based on silicon photodetectors. However, longer wavelengths also result in longer mode attenuation lengths, exacerbating the resolution problem. Hence, loss of resolution along the mode propagation direction is most acute in this widely-used SPRI configuration, making it a good point of comparison for demonstrating our work on metal surface nanostructuring to improve imaging resolution. Both 1D (lines) and 2D (pillars) grating nanostructures are studied in the modeling and experimental sections below. The dielectric material system in the case study is based on biological cells.

## 2. Numerical analysis

The role of the numerical analysis is to determine the optimal nanostructure geometry according to application-specific requirements based on 4 imaging performance metrics that are functions of the hybrid mode characteristics: 1) *Mode attenuation length*: since high spatial resolution is required to resolve fine features in cell morphology, attenuation length must be as short as possible. Mode attenuation length,  $L_x$ , is defined as the propagation distance over which mode power decreases to  $1/e$  of its steady-state value; 2) *Penetration depth into the dielectric*: since cells are relatively thick objects, measurement range into the fluid must be as deep as possible. Penetration depth,  $L_z$ , is defined as the distance into the dielectric from the interface over which the mode amplitude decreases to  $1/e$  of its value at the interface; and 3) *Measurement dynamic range or resonance contrast*: since the dielectric

material system in the case study involves a wide range of refractive indices, a large dynamic range is required. Resonance contrast is defined as the drop in output intensity at resonance relative to total internal reflection, normalized with respect to an unstructured 50 nm Au film (normalization is not required for the other metrics which are defined in absolute units); 4) *Sensitivity* is defined as the maximum change in output light intensity as a function of change in two material properties in the dielectric: volume refractive index (“bulk sensitivity”: %/RIU) and surface adlayer (biofilm) thickness (“surface sensitivity”: %/nm, relative to a 5 nm biofilm at  $n = 1.48$ ). In addition, design constraints are imposed by the available instrumentation (highest mode effective index accessible by the optical coupling system) and by the nanofabrication process (minimum feature size), as discussed below.

The numerical analysis was conducted using a custom-developed tool that combines the finite element method (FEM) with the Fourier modal method (FMM) for resource-efficient modeling of photonics devices that include periodic and aperiodic structures at different levels of scale [32]. Sources for refractive indices used in the analyses are as follows: metals (Cr and Au) measured with ellipsometry typically very close to Johnson & Christy [33], distilled water from the Sellmeier equation [34], KMPR and BK7 from manufacturer specifications (MicroChem Corp. and SCHOTT AG, respectively).

As shown in Fig. 1(a), the substrates are composed of a BK7 glass cover slip, a 3 nm Cr adhesion layer, a continuous Au film (thickness,  $h_1$ ), a nanostructured Au grating (thickness,  $h_2$ ), and distilled water as the dielectric sensing medium. Two types of grating structures (period  $\Lambda$ , width  $w$ ) are studied: lines (periodic in  $x$ , uniform in  $y$ ) and pillars (periodic in  $x$  and  $y$ ). Thickness  $h_2$  is zero for unstructured films.

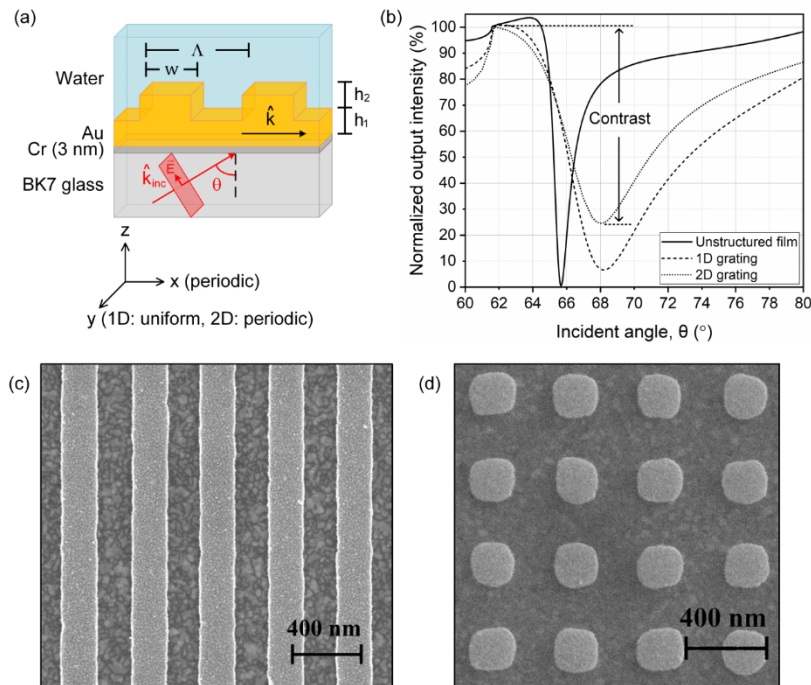


Fig. 1. (a) Schematic of the SPRI substrate thin film stack: BK7 glass cover slip – Cr adhesion layer (3 nm) – nanostructured Au film – distilled water. The nanostructured Au film is composed of a uniform bottom layer (height  $h_1$ ) and a grating top layer (height  $h_2$ , period  $\Lambda$ , width  $w$  along  $x$ ). For 1D gratings, the geometry is uniform along  $y$ , whereas 2D gratings have the same periodicity along  $x$  and  $y$ . A TM-polarized plane wave with wavevector  $k_{inc}$  is incident at the glass/metal interface at angle  $\theta$ ; (b) Modeled reflectance curves versus incidence angle for unstructured ( $h_1 = 50$  nm) and structured ( $w = 200$  nm,  $\Lambda = 400$  nm,  $h_1 = 25$  nm,  $h_2 = 25$  nm) Au films, showing the resonance contrast metric definition for the 2D grating; (c-d) SEM images of 1D and 2D nanostructured substrates with grating parameters as in (b).

A TM-polarized plane wave at  $\lambda = 830$  nm ( $k_{inc}$ ) is incident at angle  $\theta$  and totally internally reflected at the glass/metal interface. The incident light couples via optical tunneling through the metal to the hybrid SPP mode at the opposite metal/dielectric interface (Au/water) when both wavevector components along the  $x$ -axis are matched. Figure 1(b) shows modeled reflectance curves as a function of incidence angle for unstructured ( $h_1 = 50$  nm,  $h_2 = 0$  nm) and structured ( $w = 200$  nm,  $A = 400$  nm,  $h_1 = 25$  nm,  $h_2 = 25$  nm) Au films, also showing the resonance contrast metric definition in the case of the 2D grating. Figures 1(c) and (d) show SEM images of 1D and 2D nanostructured Au films fabricated by electrolithography ( $w = 200$  nm,  $A = 400$  nm).

Our numerical modeling tool calculates the complex wavevector ( $k = k' + ik''$ ) of the guided hybrid SPP mode at the metal/dielectric interface. The first two metrics (mode attenuation length,  $L_x$ , and penetration depth,  $L_z$ ) can then be calculated in the usual way from the wavevector components:

$$L_x = \frac{1}{2k''} \quad (1)$$

$$L_z = \frac{1}{\sqrt{(k')^2 - \left(\frac{2\pi n_{BK7}}{\lambda}\right)^2}} \quad (2)$$

Note that since the evanescent field profile in the dielectric above a structured film is not uniform along  $x$  (1D and 2D gratings) and  $y$  (2D gratings), neither is the penetration depth. Nevertheless, Eq. (2) gives a useful “average” value for this metric. The modeling tool also calculates output light intensity as a function of incidence angle to generate intensity vs angle transfer functions, as required to estimate resonance contrast (third metric) and bulk/surface sensitivities (fourth metric).

Though our numerical tool is more capable than existing commercial products for full 3D electromagnetic field modeling of complex structures involving different levels of scale, the modal analysis module (eigen mode expansion) is currently limited to 2D analyses (code development for extending this functionality to 3D is ongoing). Hence, the numerical analysis below of the performance metrics as a function of nanostructure geometry is based on 1D line gratings (2D space analysis), since the performance metrics are themselves derived from the hybrid mode characteristics and/or far field behavior of the structure (reflectance signal at the detector as a function of coupling to/from the hybrid mode). Nevertheless, numerical analysis of 1D line gratings yields very good insight into 2D grating design and characteristics, as confirmed by the experimental results below for both 1D and 2D gratings.

The numerical analysis of the 1D line grating structure described in Fig. 1(a) proceeded in two steps. The first step calculated the performance metrics as a function of the in-plane grating characteristics ( $w$ ,  $A$ ) while the out-of-plane grating characteristics ( $h_1$ ,  $h_2$ ) were kept constant, each equal to half the standard 50 nm thickness used in conventional SPRI with unstructured metal films at  $\lambda = 830$  nm ( $h_1 + h_2 = 50$  nm). The grating period was varied from 100 to 500 nm and the line width was varied from 50 to 450 nm, both in increments of 5 nm. The second step refined the analysis to identify the optimal out-of-plane characteristics ( $h_1$ ,  $h_2$ ). To compare modeling results with conventional SPRI systems, the analysis was also performed for unstructured Au films over a range of film thicknesses (10 nm to 50 nm). In particular, the standard 50 nm thickness used in SPR on Au films at  $\lambda = 830$  nm, yielding the highest sensitivity and contrast for an aqueous dielectric medium at this wavelength, is used as a benchmark in the discussion below.

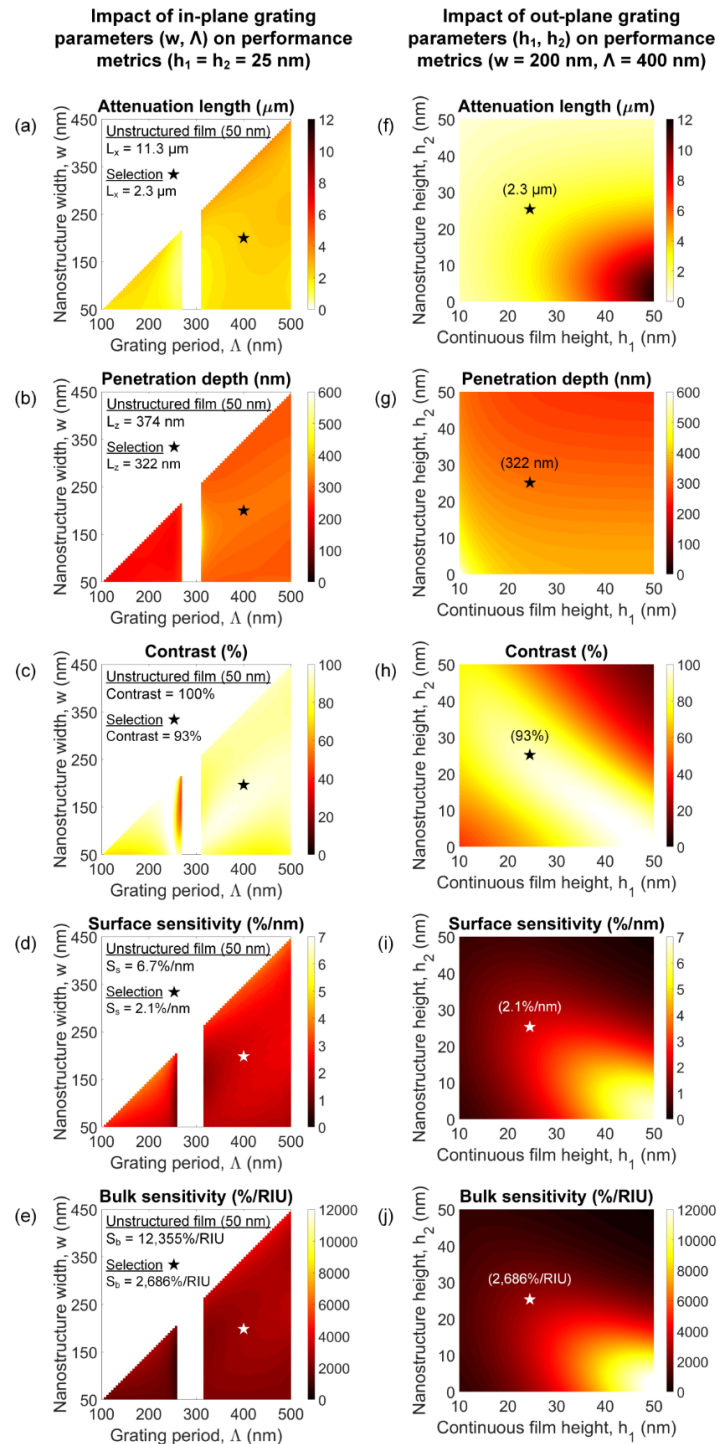


Fig. 2. (a)-(e) Modeled 2D maps of the performance metrics as a function of in-plane grating parameters ( $w$  and  $\Lambda$ ) for fixed out-of-plane parameters ( $h_1 = 25$  nm,  $h_2 = 25$  nm); (f)-(j) Modeled 2D maps of the performance metrics as a function of out-of-plane grating parameters ( $h_1$  and  $h_2$ ) for fixed in-plane parameters ( $w = 200$  nm and  $\Lambda = 400$  nm). The star markers indicate the estimated metric values for a surface nanostructure geometry of  $w = 200$  nm,  $\Lambda = 400$  nm,  $h_1 = 25$  nm,  $h_2 = 25$  nm. All results calculated for  $\lambda = 830$  nm.

Figures 2(a)-2(e) show 2D maps of the performance metrics at  $\lambda = 830$  nm as a function of in-plane grating parameters ( $w, \Lambda$ ) with  $h_1 = h_2 = 25$  nm. Due to the anti-crossing between the first order grating modes and the propagating SPP modes [28], there is a bandgap centered on a grating period of  $\sim 300$  nm. For short grating periods ( $\Lambda < 300$  nm), the hybrid mode is highly confined (short  $L_x$  and  $L_z$ ). At longer grating periods ( $\Lambda > 300$  nm) mode confinement is lower, resulting in contrast and penetration depth values comparable to an unstructured 50 nm film. Importantly, attenuation length is significantly shorter overall compared to an unstructured film, especially near the band gap. Finally, though bulk and surface sensitivities improve slightly further away from the bandgap, they are lower in general compared to an unstructured film due to the higher confinement of the hybrid SPP mode. However, this loss in sensitivity is an acceptable compromise in view of the important expected gains in imaging resolution due to the reduction in attenuation length along the direction of mode propagation.

As indicated by the star markers in Fig. 2, we chose  $w = 200$  nm and  $\Lambda = 400$  nm as a compromise between theoretical and practical considerations. From a theoretical perspective, a point closer to the bandgap, for example  $w = 100$  nm and  $\Lambda = 350$  nm, would improve spatial resolution slightly. However, such narrow structures are difficult to fabricate reliably over large areas with a lift-off process. In addition, the numerical aperture of the microscope objective imposes an upper limit on the incidence angle of the excitation light. This in turn imposes an upper limit on the effective index of the guided modes than can be excited in the structure since mode index increases with decreasing grating period. The objective used in our system (NA = 1.46) imposes a lower limit of  $\Lambda = 325$  nm on the grating period.

In the second step of the numerical analysis, the line width and period were kept constant at  $w = 200$  nm and  $\Lambda = 400$  nm while the bottom continuous film thickness ( $h_1$ ) was varied from 10 to 50 nm and the nanostructure height ( $h_2$ ) was varied from 0 nm to 50 nm, both in increments of 1 nm. Figures 2(f)-2(j) show 2D maps of the performance metrics as a function of out-of-plane grating parameters at  $\lambda = 830$  nm. As seen in Fig. 2(f), hybrid mode attenuation length improves (decreases) along the diagonal starting at the bottom-right, upwards to the top-left, due to the increasing influence of the localized mode component as the grating depth of modulation increases ( $h_2$  vs  $h_1 + h_2$ ) at constant total metal thickness ( $h_1 + h_2$ ). Conversely, Figs. 2(g)-2(j) show that contrast and sensitivity decrease along the same diagonal and direction, relative to the bottom-right corner where the influence of the propagating mode component is highest. A total metal thickness of 50 nm with a 50% grating depth of modulation ( $h_1 = h_2 = 25$  nm, see star markers in the figures), as used in the previous analysis step, yields an acceptable compromise between the two opposing tendencies. Finally, Fig. 2(h) shows that penetration depth is relatively independent of continuous film thickness while it decreases with increasing nanostructure height due to higher field confinement.

SPRI applied to biological cell imaging is relatively new and is still in its exploratory stages. Indeed, the vast majority of existing SPRI systems are used for parallel monitoring of bioassay kinetics in spotted microarrays where high sensitivity is critical while spatial resolution requirements are moderate since spot diameters are typically relatively large ( $> 100$   $\mu\text{m}$ ). In the case of cell imaging, as explained earlier, the opposite is true: sensitivity requirements are moderate while spatial resolution and contrast (dynamic range) are of primary importance. As such, the direct trade-off between these two metrics, resulting from the opposing influences of the propagating and localized components in the hybrid mode, is central to the design process seeking to optimize the surface nanostructure geometry for a particular application.

Figure 3 shows plots of contrast as a function of attenuation length at  $\lambda = 830$  nm for different configurations of the structure shown in Fig. 1. The solid back curve shows the resolution vs contrast trade-off for unstructured Au films as a function of thickness (10 nm – 50 nm), where attenuation length is 11.3  $\mu\text{m}$  and contrast is 100% for a 50 nm film. As film thickness decreases (leftward along the curve, starting from the right at 50 nm thickness), attenuation length decreases as well since the SPP mode becomes “leakier”, which also

causes contrast to decrease due to incomplete destructive interference at resonance with the uncoupled portion of the input light. The colored curves show three cases of structured metal films (1D gratings) at selected nanostructure heights ( $h_2 = 15$  nm, 25 nm, and 35 nm) over a range of bottom metal layer thicknesses ( $h_1$  increases from left to right along the curves). In each case, the particular bottom metal layer thickness corresponding to the curve apex (maximum achievable contrast for a particular value of  $h_2$ ) is indicated in the figure legend.

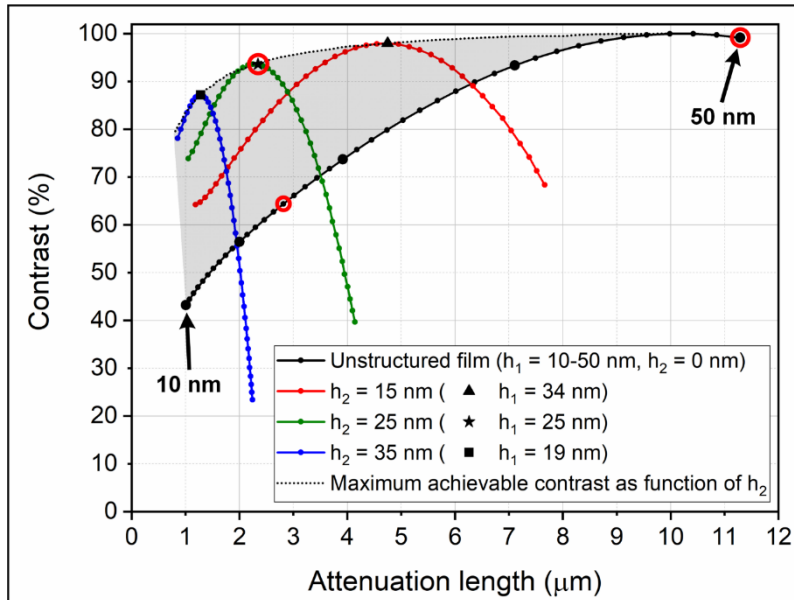


Fig. 3. Modeled contrast vs mode attenuation length at  $\lambda = 830$  nm for different configurations of the structure shown in Fig. 1. Solid black curve: unstructured Au film, thickness increases from 10 to 50 nm, left to right along the curve (small dots: 1 nm steps, large dots: 10 nm steps). Colored curves: nanostructured Au films (1D gratings,  $w = 200$  nm,  $A = 400$  nm) for 3 examples of selected nanostructure height ( $h_2 = 15$  nm, 25 nm, 35 nm) as a function of increasing bottom metal layer thicknesses from left to right along the curves, where the values of  $h_1$  at the apex of each curve (maximum contrast) are given in the legend. Dotted black line: maximum achievable contrast versus attenuation length for structured films at varying nanostructure heights  $h_2$ . The circular markers indicate the 1D nanostructured substrate configuration and two unstructured substrate configurations that were fabricated and characterized experimentally, as shown below.

Figure 3 demonstrates one of the most important results of this work, namely that surface nanostructuring can significantly improve the resolution (attenuation length) vs contrast trade-off in SPRI high-resolution imaging. The dotted black curve at the top traces the maximum achievable contrast for a given nanostructure height ( $h_2$ ) along with the corresponding attenuation length. The vertical difference between the dotted and solid black curves shows the improvement in resolution/contrast trade-off enabled by surface nanostructuring. Furthermore, the grayscale area between by the two black curves illustrates the latitude with which the imaging characteristics can be chosen. Indeed, for a particular application, the optimal surface nanostructure geometry may not be along the dotted black line at the top (maximum achievable contrast) but rather at a point between the two curves where resolution can be further improved at the price of an acceptably small loss of contrast. The apex of the green curve ( $h_1 = h_2 = 25$  nm) in Fig. 3 indicates the particular nanostructure configuration chosen for the experiments.

Another important result of this work demonstrated in the next section is that surface nanostructuring with a 2D grating (pillars) yields a further improvement in the resolution/contrast trade-off. Moreover, 2D nanostructuring has greater potential compared to

the 1D case for reducing the sensitivity gap with unstructured films, if required. Note that operating at shorter wavelengths and/or using metals with higher losses (ex: Cu) will also reduce attenuation length. However, a shorter wavelength with unstructured substrates does not significantly improve the resolution/contrast trade-off (data not shown).

### 3. Experimental results and parameter estimation

This section describes the experimental measurements acquired using both unstructured and nanostructured SPRI substrates, followed by parameter estimation of the attenuation length and contrast performance metrics from the experimental data. Since penetration depth into the dielectric is difficult to measure reliably in practice (it can be done with a scanning near-field optical microscope, but the deconvolution has a high degree of uncertainty), the actual value of this metric was not confirmed experimentally. Sensitivity measurements were not performed as the central interest here is with image spatial resolution. The SPRI imaging system used in the experiments is based on a high numerical aperture microscope objective with excitation light at  $\lambda = 830$  nm [10]. The system can simultaneously image a sample from the underside with SPRI and from the topside with brightfield or fluorescence microscopy ( $63\times$  objective).

The SPRI substrates were fabricated on BK7 glass cover slips (170  $\mu\text{m}$  thick, 22x22mm, Fisher Scientific). The Au nanostructures were fabricated with electron beam lithography and lift off. To acquire good SPRI image data for robust parameter estimation, a synthetic “target layer” incorporating a variety of shapes with sharp edges was patterned atop the metal surface of the substrates. This target layer was fabricated with 220 nm thick photoresist (KMPR, MicroChem Corp., similar to SU8 but with higher resistance to fissuring) patterned with UV lithography to expose the metal in orifices of various shapes. The cover slips were first cleaned with a solvent (acetone, isopropyl alcohol, distilled water, 5 min sonication per step) and dried with  $\text{N}_2$  prior to deposition of the uniform bottom metal film in an e-beam evaporator (3 nm Cu, 25 nm Au, IntlVac, USA). A PMMA bilayer (bottom: LMW 4% in anisole, top: HMW 2% in anisole) was spin-coated atop the Au film (90 s soft bake on hot plate at 180°C per layer) and exposed to a 20 kV e-beam for patterning the 1D and 2D gratings in 200x200  $\mu\text{m}^2$  areas. The PMMA resist was developed in a 9:1 isopropyl alcohol-water solution (1 min), rinsed in water (30 sec), and dried with  $\text{N}_2$ . A second 25 nm Au film was then deposited with the e-beam evaporator and the Au nanostructures were revealed by lift-off in a solvent (Microposit Remover 1165, MicroChem Corp.). KMPR (KMPR1005, 15% dilution with SU8 thinner, MicroChem Corp.) was spin-coated on the nanostructured samples, soft baked (1 min, hot plate at 110 °C), UV exposed (Model 806, OAI) for 10 sec (120 mJ/cm<sup>2</sup>), soft baked (1 min, hot plate at 110 °C), developed in solvent (MicroChem SU-8 Developer, Isopropyl alcohol, water, 30 sec per step) and dried with  $\text{N}_2$ .

The substrates were inserted into the SPRI imaging system and covered by a microfluidic chamber filled with distilled water. The “BK7/Cr/Au/KMPR/water” and “BK7/Cr/Au/water” film stacks will form distinct waveguide structures supporting SPP modes of different effective indices according to whether the dielectric in contact with the metal is either water ( $n_{\text{water}} = 1.328$ ) or resist ( $n_{\text{KMPR}} = 1.555$ ). As a result, excitation light at a fixed angle of incidence  $\theta$  will result in different output light intensity levels for the two cases due to differences in input/output coupling efficiency to/from the guided modes. For example, for the 1D grating geometry discussed above ( $w = 200$  nm,  $A = 400$  nm,  $h_1 = 25$  nm,  $h_2 = 25$  nm), the difference in output light intensity at  $\theta = 68^\circ$  and  $\lambda = 830$  nm between the two film stacks is 85.5% (normalized with respect to an unstructured 50 nm Au film, as per the contrast metric definition).

Figure 4(a) shows the brightfield image of a cross-shaped orifice in the target layer where the dielectric atop the metal is KMPR outside the cross and water inside the cross. Figures 4(b)-4(e) show SPRI images at  $\lambda = 830$  nm of the target patterned onto unstructured Au films (b:  $h_1 = 50$  nm, c:  $h_1 = 25$  nm) and nanostructured Au films (d: 1D lines, e: 2D pillars,  $h_1 = 25$

nm,  $h_2 = 25$  nm,  $w = 200$  nm,  $\Lambda = 400$  nm). In the SPRI images, dark pixels indicate strong coupling of the excitation light to the SPP mode which results in low reflectivity from the substrate whereas light pixels indicate weak coupling which results in high reflectivity. The direction of mode propagation is from left to right along the horizontal. The SPRI images were normalized by subtracting the dark image and dividing by the average intensity in a small uncoupled zone common to all images. Figure 4(b) shows the resolution anisotropy problem clearly: horizontal edges are clearly resolved whereas vertical edges perpendicular to the mode propagation direction appear blurred. The SPR image sequence in Fig. 4 illustrates increasing improvements in spatial resolution first by reducing the metal film thickness to increase mode leakage in an unstructured substrate [Figs. 4(b) and (c)], then with 1D nanostructuring [Fig. 4(d)], and finally with 2D nanostructuring [Fig. 4(e)].

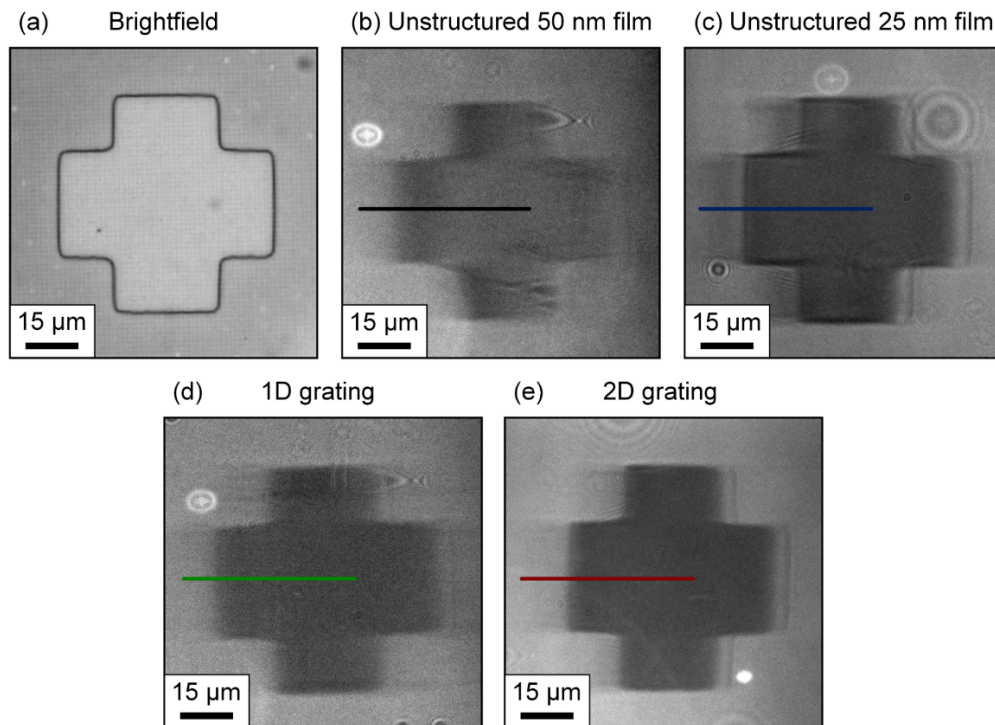


Fig. 4. (a) Brightfield image of a cross-shaped orifice in the synthetic target layer: the dielectric atop the metal outside the cross is KMPR and water inside the cross; (b-e) Normalized SPRI images at  $\lambda = 830$  nm of the cross patterned atop: unstructured Au films (b: 50 nm, c: 25 nm) and nanostructured Au films (d: 1D lines, e: 2D pillars,  $h_1 = 25$  nm,  $h_2 = 25$  nm,  $w = 200$  nm,  $\Lambda = 400$  nm). Mode propagation is from left to right. The horizontal line overlays indicate the line profiles plotted in Fig. 5.

Though our modeling tool is particularly efficient, it is nevertheless computationally demanding as with all such field-based numerical tools for solving Maxwell's equations over a discretized space. Since parameter estimation from experimental data typically involves iterative multi-variate non-linear minimization, a more practical choice for this task is a simpler physics-based parametric model that relates the parameters one wishes to estimate with the observable variables in the data. Equation (3) expresses the light intensity reflected from an SPR substrate as a function of the incident light wavevector, angle of incidence, and SPP mode wavevector [6, 11, 13]. This parametric model expresses a line profile of reflected intensity along the direction of mode propagation,  $I(x)$ , following a step change in dielectric index at  $x = 0$  that increases the coupling level between the incident light and the SPP mode:

$$I(x) = (I_{\max} - I_{\min}) e^{-2k''x} \cos(\Delta k'x) + I_{\min} \quad (3)$$

where  $I_{\max}$  and  $I_{\min}$  are the steady-state reflected light intensities before and after the index step change,  $k''$  is the imaginary part of the surface mode wavevector  $k = k' + ik''$  supported by the waveguide structure following the step, and  $\Delta k'$  is the difference between the real part of the mode wavevector and the (purely real) input light wavevector ( $k_{inc}$ ) incident at angle  $\theta_{inc}$ :

$$\Delta k' = k' - k_{inc}' = k' - \frac{2\pi}{\lambda} n_{BK7} \sin(\theta_{inc}) \quad (4)$$

As seen along the horizontal lines from left to right in Figs. 4(b)-4(e), the reflected intensity drops to a minimum following the abrupt dielectric change above the metal from KMPR to water. The coupling between the incident light and the guided mode requires a finite distance to reach steady state as expressed by the exponential in Eq. (3). This in turn explains the exponential decay in reflected light intensity in the direction of mode propagation following a step change in dielectric refractive index and why resolution along this direction is limited by the attenuation length [Eq. (1)] rather than diffraction. The sinusoidal modulation of the exponential in Eq. (3) is characteristic of the destructive interference underlying the coupling process. As a result, “fringes” or “ringing” appear along edges perpendicular to the direction of mode propagation, contributing significantly to the degradation of perceived spatial resolution in high-resolution SPRI images [9,13]. To fit the line profile data from an image to Eq. (3),  $I_{\max}$  and  $I_{\min}$  are first estimated by calculating average pixel intensities over homogeneous areas on either side of the step. Equation (3) is then fitted to the data by constrained minimization to obtain estimates of the free parameters (wavevector components, incidence angle, and relative location of the origin  $x = 0$ ), where constraints on the fitting domains correspond to narrow ranges about nominal values determined from the numerical modeling (wavevector components), instrumentation settings (incidence angle), and the image data (location of the origin). The attenuation length and penetration depth metrics are then calculated from the fitted mode wavevector components with Eqs. (1) and (2).

Figure 5 shows line profiles of reflected intensity in the direction of the mode propagation from left to right along the horizontal line overlays in Figs. 4(b)-4(e), where mode coupling to the excitation light goes from weakly coupled (KMPR top layer, high output intensity) to strongly coupled (water top layer, low output intensity). The experimental data are plotted with solid lines (black and blue: unstructured film, green and red: nanostructured films) and the parametric fits are plotted with dotted lines in the corresponding colors. The parametric model shows a good fit with the exception of the soft shoulder at the start of the intensity drop that is not explicitly modeled by Eq. (3) [6, 11]. The large undershoot in the line profiles for the unstructured films is due to the sinusoidal modulation term in Eq. (3). In the structured film profiles, however, no undershoot is visible. Interestingly, the effect is not symmetrical. Indeed, as seen on Fig. 4(e), the modulation is absent for the weak-to-strong coupling transition at the leftmost edge of the cross pattern and present at the strong-to-weak coupling transition at the rightmost vertical edge of the cross pattern. This asymmetry is likely due to differences in the way the multiple wave components involved combine to reach steady state conditions after an abrupt change in coupling conditions (weak to strong coupling: buildup to a guided mode, destructive interference with the incident light; strong to weak coupling: diffusion of the guided light, decay back to uncoupled conditions, incomplete interference with the incident light), combined with a shorter mode attenuation length.

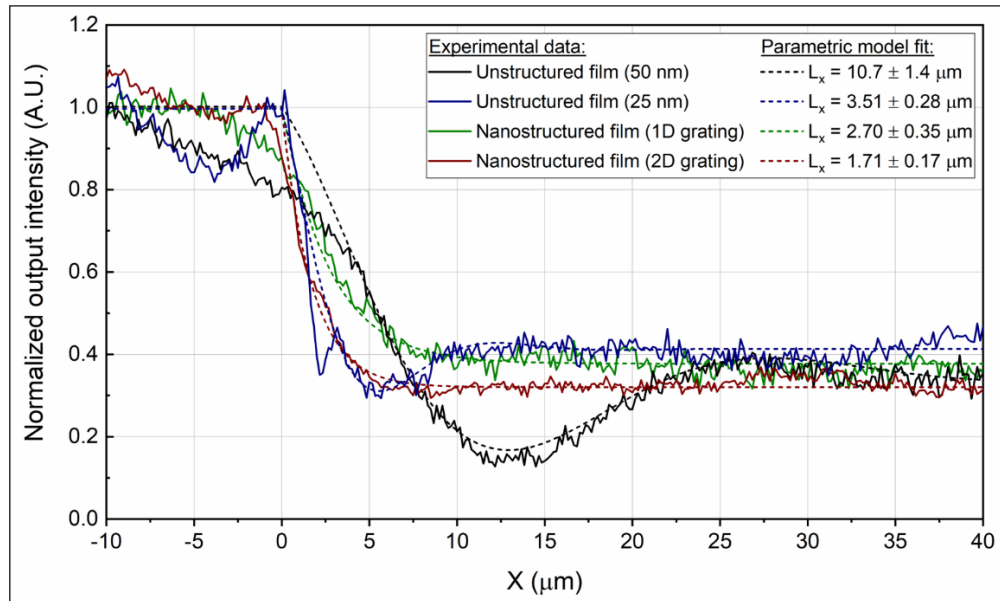


Fig. 5. Plots of reflected intensity line profiles in the direction of mode propagation for the line overlays shown in Figs. 4(b)-4(e). Experimental data: solid lines, parametric model fits: dotted lines.

Parametric model parameter fits averaged across 10 neighboring horizontal lines in the images yielded estimates of  $L_x = 10.7 \pm 1.4 \mu\text{m}$  and  $L_x = 3.51 \pm 0.28 \mu\text{m}$  for the unstructured films ( $h_l = 50 \text{ nm}$  and  $25 \text{ nm}$ , respectively) and  $L_x = 2.70 \pm 0.35 \mu\text{m}$  and  $L_x = 1.71 \pm 0.17 \mu\text{m}$  for the structured films (1D and 2D gratings, respectively). The estimates for the unstructured films and 1D grating are in close agreement with the numerical analysis from the previous section ( $L_x = 11.3 \mu\text{m}$ ,  $L_x = 2.8 \mu\text{m}$ ,  $L_x = 2.3 \mu\text{m}$ , respectively). The 2D nanostructured film results in a 6.3-fold decrease in attenuation length over the 50 nm unstructured film and a 2-fold decrease over the 25 nm unstructured film, with commensurate increases in spatial resolution. A straight comparison of attenuation lengths tells only part of the story, however, as the sinusoidal perturbations in the line profiles, which also contribute significantly to the degradation in perceived spatial resolution, is absent for the structured films at transitions from weak to strong mode coupling.

Figure 6 shows the results of an experiment on a more complex target layer designed to characterize the impact of nanostructuring on spatial resolution in SPRI in terms of feature size and separation between objects.

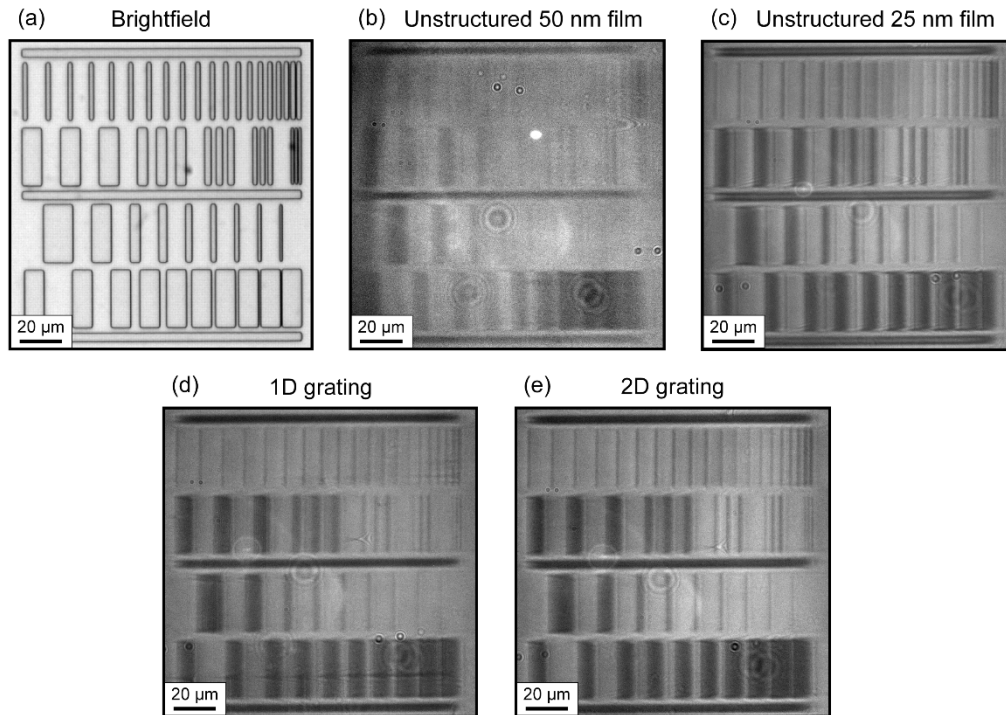


Fig. 6. Resolution test chart patterned in the synthetic target layer imaged with (a) brightfield and SPRI on unstructured (b: 50 nm, c: 25 nm) and nanostructured (d: 1D lines, e: 2D pillars,  $h_1 = 25$  nm,  $h_2 = 25$  nm,  $w = 200$  nm,  $\Lambda = 400$  nm) Au films at  $\lambda = 830$  nm. In (b)-(e), light grey (weak coupling to the hybrid mode) indicates KMPR atop the metal and dark grey (strong coupling) indicates water-filled orifices in the target layer. Mode propagation direction is left to right horizontally, i.e. perpendicular to the vertical edges. Top row in the images: 2  $\mu$ m wide lines with variable spacing (10 to 1  $\mu$ m, in 0.5  $\mu$ m steps). Second row: groups of 3 lines having equal width and spacing (10, 5, 3, 2, 1  $\mu$ m). Third row: lines of variable width (15, 10, 5, 4, 3, 2.5, 2, 1.5, 1  $\mu$ m) at fixed spacing (10  $\mu$ m). Fourth row: inverse of previous row (10  $\mu$ m fixed line width, variable spacing).

Figure 6(a) shows a brightfield image of the sample with rectangle-shaped orifices of varying widths and spacings in the KMPR target layer. Figures 6(b)-6(e) show normalized SPRI images of the pattern on unstructured (b: 50 nm, c: 25 nm) and nanostructured (d: 1D grating, e: 2D pillars, grating geometry is identical to the structure shown in Fig. 4) Au films. Mode propagation direction is along the horizontal from left to right. The finest features in the target layer, for example the 2  $\mu$ m lines (top row) and the 1  $\mu$ m lines separated by 1  $\mu$ m (second row, RHS), are distinctly resolved in Fig. 6(e) only, in a clear demonstration of the image resolution improvement due to the 2D grating surface nanostructuring.

#### 4. Conclusion

This work shows that metal surface nanostructuring significantly improves the inherent trade-off in plasmonics imaging between spatial resolution and other performance metrics compared to the smooth metals films used in most SPRI systems, enabling sub-micrometer resolution near-field label-free imaging in both axes with high contrast. A detailed numerical analysis of 1D grating nanostructured substrates based on performance metrics relevant to imaging (attenuation length, penetration depth into the dielectric, resonance contrast, bulk and surface sensitivities) is used to characterize SPRI performance as a function of nanostructure geometry. Parametric fits to the experimental data obtained with fabricated devices show excellent agreement with the numerical modeling. Experimental results further show that 2D surface nanostructuring with nano-pillars provides additional imaging performance

improvement over 1D line gratings. Note that while spatial resolution in SPRI with unstructured metal surfaces can be improved in the direction of mode propagation simply by increasing mode leakage using thinner metal films (see results above for a uniform 25 nm Au film) or by increasing mode losses using higher-loss metals (ex: Cu), such purely “detuning-based” solutions potentially result in severe reductions in measurement sensitivity and image contrast. Using the proposed nanostructuring-based design methodology, however, overall imaging performance is superior and the surface geometry can be optimized according to application-specific requirements and fabrication constraints.

### **Funding**

Natural Sciences and Engineering Research Council of Canada (NSERC) (RGPIN-2015-05188).

### **Acknowledgments**

This work was supported by the Natural Sciences and Engineering Research Council of Canada (NSERC) with Discovery Grants for M.C. and P.G.C. F.A.B. is supported by a doctoral scholarship from the Fonds de Recherche du Québec - Nature et Technologies (FRQNT) and by a French doctoral contract (MESRI) with the Université Paris-Saclay. LN2 is an international laboratory (Unité Mixte Internationale UMI 3463) jointly managed by French CNRS and the Université de Sherbrooke as well as Université de Lyon (ECL, INSA de Lyon, CPE) and the Université Grenoble Alpes (UGA). LN2 is associated to the French national nanofabrication network RENATECH and is also financially supported by FRQNT. The authors thank C. Colin and T. Söllradl for help in electrolithography and experimental acquisition.